

## ENGINEERING

# Millimeter-scale magnetic implants paired with a fully integrated wearable device for wireless biophysical and biochemical sensing

Ji Wan<sup>1,2†</sup>, Zhongyi Nie<sup>1†</sup>, Jie Xu<sup>1</sup>, Zixuan Zhang<sup>3</sup>, Shenglian Yao<sup>4</sup>, Zehua Xiang<sup>1,2</sup>, Xiang Lin<sup>1</sup>, Yuxing Lu<sup>5</sup>, Chen Xu<sup>1,6</sup>, Pengcheng Zhao<sup>1,2</sup>, Yiran Wang<sup>1</sup>, Jingyan Zhang<sup>1</sup>, Yaozheng Wang<sup>1,2</sup>, Shaotong Zhang<sup>7</sup>, Jinzhao Wang<sup>5</sup>, Weitao Man<sup>8</sup>, Min Zhang<sup>3</sup>, Mengdi Han<sup>1\*</sup>

Implantable sensors can directly interface with various organs for precise evaluation of health status. However, extracting signals from such sensors mainly requires transcutaneous wires, integrated circuit chips, or cumbersome readout equipment, which increases the risks of infection, reduces biocompatibility, or limits portability. Here, we develop a set of millimeter-scale, chip-less, and battery-less magnetic implants paired with a fully integrated wearable device for measuring biophysical and biochemical signals. The wearable device can induce a large amplitude damped vibration of the magnetic implants and capture their subsequent motions wirelessly. These motions reflect the biophysical conditions surrounding the implants and the concentration of a specific biochemical depending on the surface modification. Experiments in rat models demonstrate the capabilities of measuring cerebrospinal fluid (CSF) viscosity, intracranial pressure, and CSF glucose levels. This miniaturized system opens the possibility for continuous, wireless monitoring of a wide range of biophysical and biochemical conditions within the living organism.

## INTRODUCTION

Implantable sensors can measure a diverse array of information within the body (1–6), including electrophysiology (7–9), biomechanics (10–13), and concentrations of neurotransmitters and other biomarkers (14–16) to support the prevention and treatment of various diseases. These sensors exhibit changes in voltage, current, resistance, or capacitance to reflect the biophysical and biochemical conditions (17–20) but must rely on transcutaneous wires for data acquisition or signal transmission. In many cases that require health monitoring (e.g., epilepsy, diabetes, and heart failure) (21–24), implantable sensors should (i) transmit the signals outside the body in a wireless fashion, to avoid infection and inflammation caused by wires (25, 26), and (ii) feed the signals into data acquisition systems with miniaturized dimensions, to support measurement in settings outside of hospital or laboratory without bulky instruments (27).

However, current solutions to meet the above requirements rely on commercial chips, such as Bluetooth or near-field communication system-on-chips (SoCs), that pose challenges in minimally invasive insertion, biocompatibility, and power supply (28–30). Although implantable sensors based on inductor-capacitor (LC) resonant circuits and ultrasonic backscatter represent alternative solutions to reduce

the dimensions of implantable sensors or to eliminate batteries, they demand bulky external acquisition systems (e.g., network analyzers, ultrasound probes, reading coils, and lock-in electronics) that are not suitable for wearable applications (text S1) (31–34).

Here, we present a set of chip-less, battery-less magnetic implants with overall dimensions in millimeter scale. The implants can wirelessly communicate with a fully integrated centimeter-scale wearable device through a magnetic field, to enable multimodal sensing of biophysical and biochemical signals. Key components of an implant involve a micro-magnet to generate an alternate magnetic field during vibration, a soft, elastomeric membrane to improve the vibration amplitude, and surface coatings to selectively absorb targeted biochemicals. The chip-less and battery-less nature of the implant promotes its biocompatibility. In vivo experiments in rat models prove that the miniaturized system (i.e., the millimeter-scale implants and the centimeter-scale wearable device) can measure cerebrospinal fluid (CSF) viscosity, intracranial pressure (ICP), and CSF glucose concentration wirelessly, with additional capability in real-time display on mobile terminals. This system opens avenues to long-term, continuous monitoring of a variety of signals related to health status, with the potential to expand to wireless sensing of many other biochemicals and biomolecules through surface modifications.

## RESULTS

### Working principle of the miniaturized system

As shown in Fig. 1A, we developed a miniaturized system that pairs a chip-less (35), battery-less magnetic implant on a millimeter scale with a fully integrated wearable device (36) mounted at the skin surface. The wearable device can produce a pulsed magnetic field to wirelessly excite the large amplitude vibration of the magnetic implant. The subsequent damped vibration of the magnetic implant generates a dynamic magnetic field that can be captured by magnetic sensors integrated in the wearable device. These analog signals are then

Copyright © 2024 The Authors, some rights reserved; exclusive licensee American Association for the Advancement of Science. No claim to original U.S. Government Works. Distributed under a Creative Commons Attribution NonCommercial License 4.0 (CC BY-NC).

<sup>1</sup>National Key Laboratory of Science and Technology on Micro/Nano Fabrication, Department of Biomedical Engineering, College of Future Technology, Peking University, Beijing, China. <sup>2</sup>School of Integrated Circuits, Peking University, Beijing, China. <sup>3</sup>School of Electronic and Computer Engineering, Peking University, Shenzhen, China. <sup>4</sup>School of Materials Science and Engineering, University of Science and Technology Beijing, Beijing, China. <sup>5</sup>Department of Bigdata and Biomedical AI, College of Future Technology, Peking University, Beijing, China. <sup>6</sup>Academy for Advanced Interdisciplinary Studies, Peking University, Beijing, China. <sup>7</sup>Yuanpei College, Peking University, Beijing, China. <sup>8</sup>Department of Neurosurgery, Beijing Tsinghua Changgung Hospital, School of Clinical Medicine, Tsinghua University, Beijing, China.

\*Corresponding author. Email: hmd@pku.edu.cn

†These authors contributed equally to this work.

digitized and transmitted to a mobile terminal via Bluetooth for real-time display and further analysis (fig. S1). Specifically, the wearable part consists of a copper coil (wire diameter: 100  $\mu\text{m}$ , turns: 1000) that converts a pulse current into a magnetic field, a tunnel magnetoresistance (TMR; text S2 and fig. S2) sensor that measures the magnetic field generated by the magnetic implant, four Hall sensors for localization of the magnetic implant, a Bluetooth SoC that communicates with a mobile terminal wirelessly, a rechargeable lithium-ion battery for onboard power supply (capacity: 1200 mAh, voltage: 7.4 V), and a

soft encapsulation layer in silicone (Fig. 1B). The magnetic implant includes a micro-magnet (diameter: 1.5 mm, height: 0.8 mm) coated with a layer of parylene-C (thickness: 10  $\mu\text{m}$ ; text S3), an elastic membrane in polydimethylsiloxane (PDMS; diameter: 6 mm, thickness:  $\sim 40$   $\mu\text{m}$ ), and a PDMS cavity substrate (diameter: 6 mm, height: 2 mm, cavity diameter: 5.5 mm, cavity height: 1 mm). The micro-magnet is located at the center of the elastic membrane, and the membrane bonds to the cavity substrate to allow for large amplitude vibration under coil excitation (Fig. 1C and figs. S3 to S5).

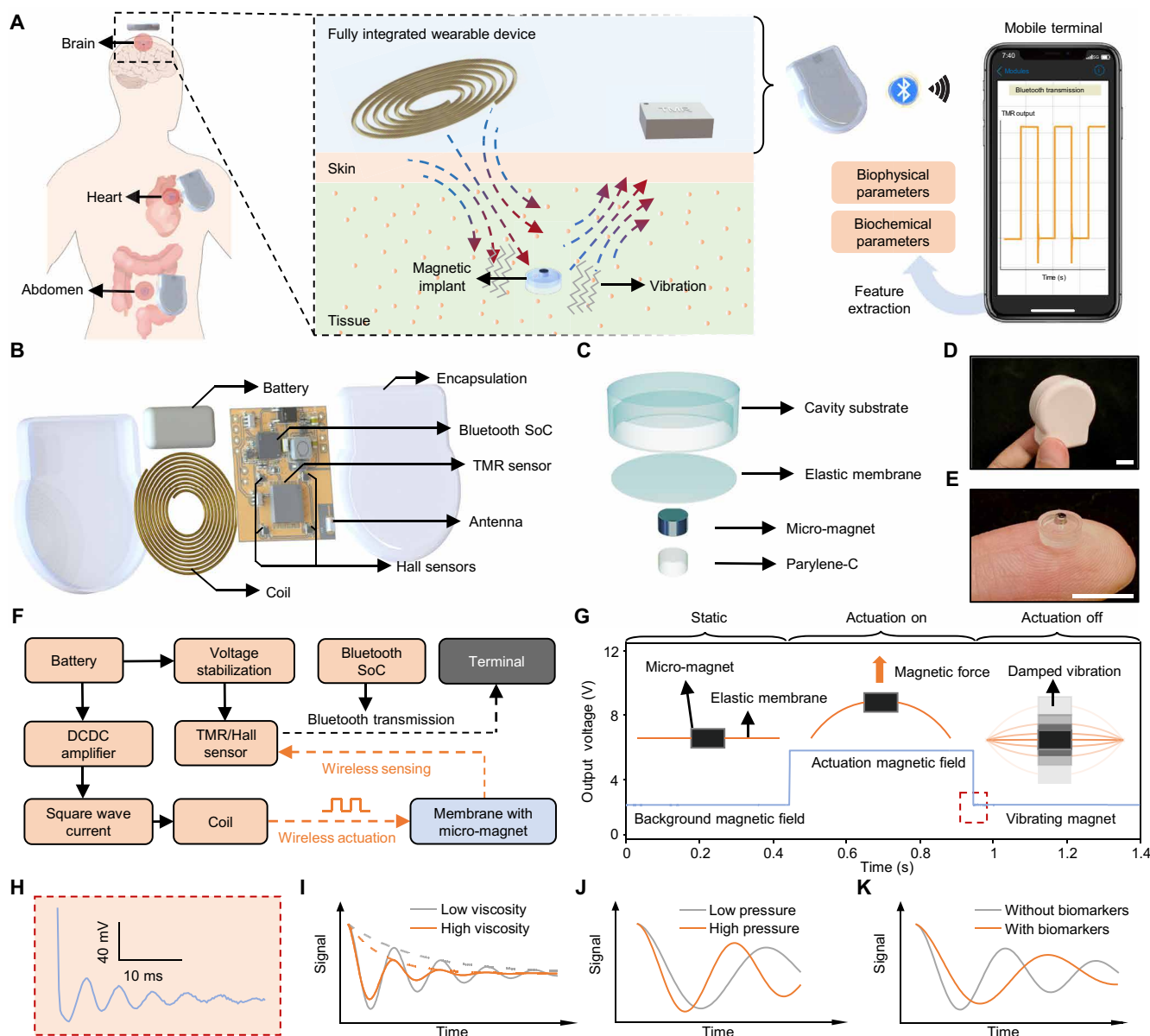


**Fig. 1. Design and working principle of the millimeter-scale magnetic implants and fully integrated wearable device.** (A) Schematic illustrations of the two-way wireless communication between the millimeter-scale magnetic implant and the fully integrated wearable device, and the data acquisition and processing in the mobile terminal. (B and C) Exploded schematic illustrations of the wearable device (B) and magnetic implant (C). (D and E) Optical images of the wearable device (D) and magnetic implants (E). Scale bars, 1 cm. (F) Block diagram of the circuit of the fully integrated wearable device for wireless actuation and sensing. (G) Schematic illustration of the motions of the micro-magnet, and corresponding vibration signals measured from the wearable device. (H) A magnified view of the vibration waveform depicted within the dashed red box in (G). (I to K) Schematic illustrations of the vibration waveforms under different viscosities (I), pressures (J), and concentrations of a specific biomarker (K). TMR, tunnel magnetoresistance; DCDC, direct current to direct current.

Figure 1 (D and E) outlines optical images of the centimeter-scale wearable device and the millimeter-scale magnetic implant. In the wearable device, a voltage stabilization module ensures a steady 7.4-V voltage for the TMR sensor, the Hall sensors, and the Bluetooth SoC. A direct current to direct current transformer boosts the battery output to 15 V for the coil to provide a sufficient magnetic field for exciting the magnetic implant. The Bluetooth SoC and an optocoupler switch modulate the 15-V voltage into a square wave with a frequency of 4 Hz. The coil converts this alternate voltage into a magnetic field with a peak intensity of 4.09 mT at a distance of 5 mm to excite the magnetic implant periodically (Fig. 1F, figs. S6 and S7, and movie S1). As estimated in text S4 and fig. S8, the wearable device can function continuously for more than 1 day when powered by a coin battery (capacity: 240 mAh) and operating at a sampling rate of 0.1 Hz (text S4 and fig. S8).

During operation, a programmed alternating magnetic field generated from the wearable device periodically drags and releases the micro-magnet of the implant (Fig. 1G and figs. S9 and S10). The elastic and low-modulus membrane of the implant enables large amplitude and nonlinear damped vibration after release (Fig. 1H). The initial vibration amplitude reaches 0.4 mm under a pulse voltage of 15 V (distance between the wearable device and magnetic implant: 5 mm), two orders of magnitude larger than those of conventional microelectromechanical systems (MEMS) (fig. S11) (37, 38). As shown in Fig. 1H, a TMR sensor captures the variations of magnetic field wirelessly with high signal-to-noise ratios (SNRs) and produces a distinctive damped vibration signal upon the release of the micro-magnet without being affected by the presence of intermediate medium materials (fig. S12). The SNRs of the first cycle of vibration reach 28 dB at a distance of 5 mm and 20 dB at a distance of 9 mm (figs. S13 and S14). Increasing the dimension of the magnet can guarantee high SNR at further distances. As an example, a millimeter-scale magnetic implant (total diameter: 8 mm, diameter of the magnet: 2.5 mm) can generate sufficient variations of a magnetic field at a distance of 30 mm (fig. S15).

The large amplitude, damped vibration signal comprises a rich set of physical and chemical information related to the environments surrounding the magnetic implant. First, viscosity holds immense value in the analysis of blood lipids and body fluids (39, 40). For a magnetic implant with either a sealed or an open cavity (figs. S2 and S16), a surrounding environment with larger viscosity accelerates the attenuation of its vibrations (Fig. 1I). Second, pressure, such as ICP, intraocular pressure, blood pressure, and abdominal pressure, represent important parameters in the realm of implantable sensing. For a magnetic implant with a sealed cavity, an elevation in its surrounding pressure deforms the elastic membrane. This buckled membrane exhibits a stiffening effect and leads to an increase in its vibration frequency (41, 42) as depicted in Fig. 1J. Third, surface modifications on the parylene-C encapsulation or the elastic membrane enable selective binding of the target analyte through protein, nucleic acid, or cells. As the concentration of a specific biomarker increases, more absorption occurs at the surface, leading to an increment of the mass of the membrane. This heavier membrane decreases the vibration frequency, as illustrated in Fig. 1K (43, 44).

### Wireless, multiplexed sensing of physical and chemical conditions

To verify the illustrations in Fig. 1 (I to K), we perform finite element analysis (FEA) and experimental measurements of different magnetic

implants designed for sensing viscosity, pressure, and glucose concentration. Figure 2 (A and B) illustrates the vibrations of the magnetic implant in liquid environments with different viscosities. As viscosity increases, the damping force exerted on the micro-magnet becomes stronger, resulting in a faster decay rate. In the FEA model, altering the viscosity from 3.5 to 4.5 centipoise (cP) accelerates the attenuation of the vibration signal, with a fitted damping factor increasing from 56.68 to 81.47 (Fig. 2A, fig. S17A, and movie S2). The experimental setup exploits mixtures of glycerol-water solutions with varying proportions to create liquid environments with different viscosities. Similar to the FEA, a mixture of 49% glycerol and 51% water (corresponding to a viscosity of 4.787 cP) enhances the damping of the magnetic implant (fitted damping factor: 100.53), compared with a mixture of 42% glycerol and 58% water (corresponding to a viscosity of 3.466 cP, fitted damping factor: 93.86; Fig. 2B and figs. S17B and S18A).

Figure 2 (C and D) shows the responses of a magnetic implant with a sealed cavity (internal pressure: 1 atm) under different external pressures (text S5). FEA results indicate that a pressure of 2 kPa deforms the membrane (thickness: 40  $\mu\text{m}$ , diameter: 5.5 mm) downward, with a displacement of 0.36 mm (Fig. 2C and fig. S19). The membrane under various pressures exhibits different effective stiffnesses and deformations. Therefore, pulling the micro-magnet upward by an external magnetic field (intensity: 4.09 mT at a distance of 5 mm) and releasing it by erasing the magnetic field result in a damped vibration of the micro-magnet along with the elastic membrane (movie S3). In experiments, we simulate the pressure of body fluids using a liquid environment and adjust the pressure through the height of the liquid level (fig. S20). The testing results reveal that a pressure increase from 3 to 5 kPa raises the vibration frequency of the first cycle from 151.63 to 160.51 Hz (Fig. 2D and fig. S18B).

To achieve wireless sensing of glucose levels, we use chemical modifications on the surface of the micro-magnet to enable specific adsorption of glucose. The modification exploits a vertical dense array of multiwalled carbon nanotubes (MWCNTs) (45) to increase the overall surface area, thereby boosting the total amount of glucose absorbed on the micro-magnet (fig. S21). The MWCNTs bond to the micro-magnet with an adhesive layer in Ecoflex Gel. Vibration tests for more than one million cycles verify the strong bonding between the MWCNTs and the micro-magnet (fig. S22). Concanavalin A (Con-A) modification on the MWCNTs enables specific binding of glucose (Fig. 2E) (46). The Raman spectra of the MWCNTs material revealed distinct peaks near 1345  $\text{cm}^{-1}$  (D peak), 1573  $\text{cm}^{-1}$  (G peak), and 2679  $\text{cm}^{-1}$  (2D peak). Comparing the results to the unmodified MWCNTs, after 1-pyrenebutanoic succinimidyl ester (PBSE) modification, a peak emerged around 1623  $\text{cm}^{-1}$ , which can be attributed to the resonance of the pyrene moiety (47). This peak provides evidence of PBSE attachment to the MWCNTs. Furthermore, the presence of three new peaks near 2905.2  $\text{cm}^{-1}$  after Con-A incubation indicates the successful attachment of Con-A (Fig. 2F) (48). Here, the magnetic implant adopts an open-cavity design to decouple the influence of pressure (fig. S23). On the basis of this magnetic implant, a higher concentration of glucose leads to a larger mass of the micro-magnet and lower vibration frequency. FEA results in Fig. 2G and movie S4 reveal a decrease in vibration frequency as the mass increases. Experiments in Fig. 2H and figs. S24 and S18C show a similar trend. As the glucose concentration varies from 2 to 30 mM, the vibration frequency decreases from 118.9 to 116 Hz. The surface modification of Con-A endows a high selectivity to glucose over sodium ions,

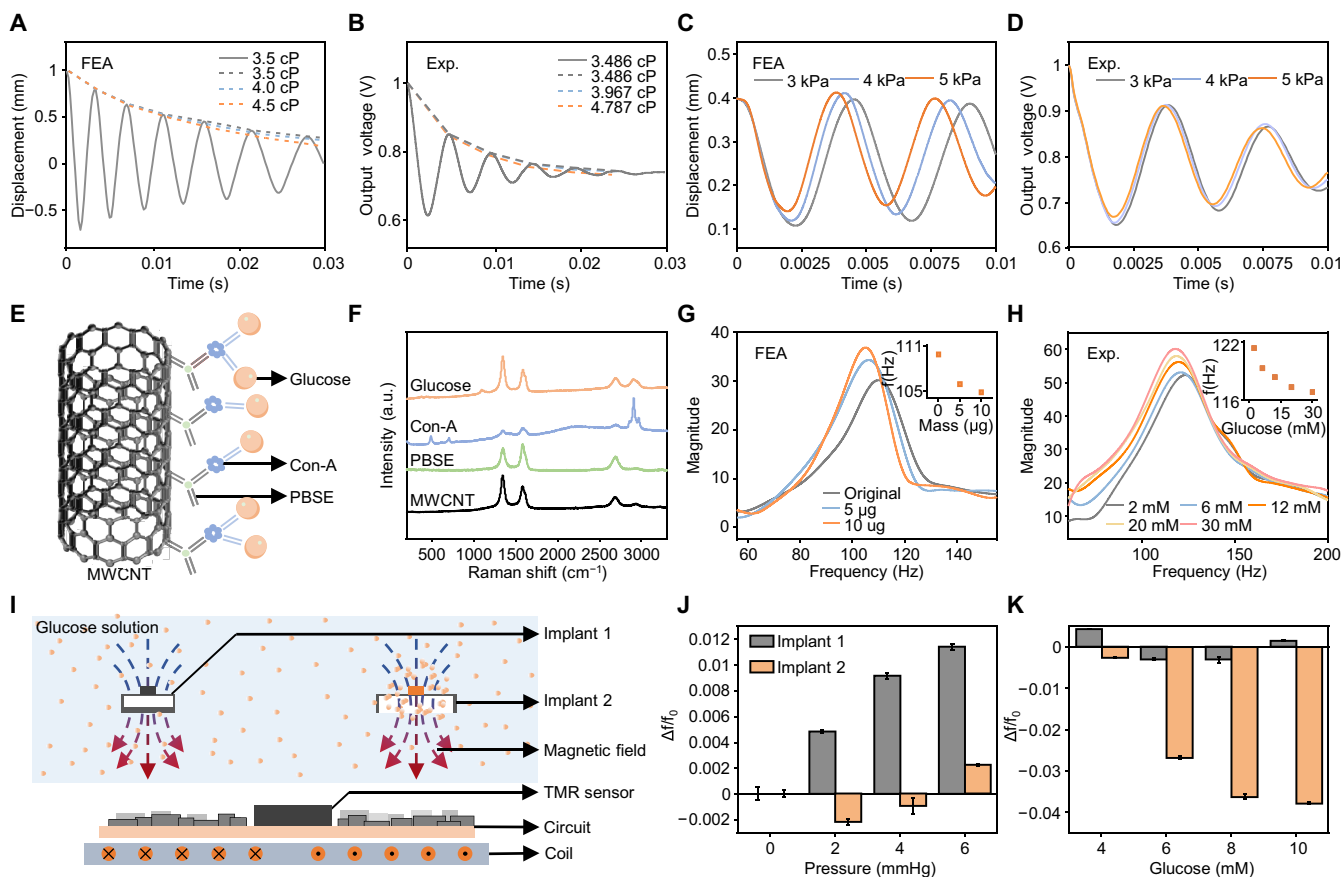


**Fig. 2. Responses of the magnetic implants under different physical and chemical conditions.** (A and B) FEA predictions (A) and experimental measurements (B) of the vibrations of the magnetic implants (sealed cavity) under different viscosities. (C and D) FEA predictions (C) and experimental measurements (D) of the vibrations of the magnetic implant (sealed cavity) under different pressures. (E) Schematic illustration of the multiwalled carbon nanotubes (MWCNTs) modified with 1-pyrenebutanoic succinimidyl ester–concanavalin A (PBSE-Con-A) for selective binding of glucose molecules. (F) Raman spectroscopy analysis of the Con-A–modified MWCNTs. (G and H) FEA predictions (G) and measured vibrations (H) of the magnetic implant (open cavity) with different adhesion masses and different glucose concentrations (fast Fourier transform, FFT of the vibration). The insets show the relationship between frequency and adhesion masses or glucose concentration. (I) Schematic illustration of two magnetic implants used for multiplexed sensing of pressure and glucose concentration. (J and K)  $\Delta f/f_0$  of the two magnetic implants for multiplexed sensing of pressure (J) and glucose concentration (K). Error bars correspond to the calculated SD from five measurements.

potassium ions, and lactic acid (fig. S25). Besides glucose, we demonstrate wireless detection of albumin and human immunoglobulin G (IgG) by modifying MWCNTs with antibodies (fig. S26). The results prove the potential of magnetic implants in wireless sensing of many biochemicals and biomolecules.

The above working principles underpin the capabilities of the magnetic implant in wireless sensing of viscosity, pressure, and glucose concentration. The elastic feature of the membrane enhances the amplitude of vibration, approximately 1.0 mm for viscosity and pressure (sealed cavity) and 0.2 mm for glucose test (open cavity; fig. S27). Such large amplitudes of vibration create a larger variation of the magnetic field to facilitate measurement using fully integrated, miniaturized wearable devices in unshielded environments. However, the large amplitude renders a nonlinear feature of the vibration, which complicates the FEA and analytical analysis. For example, in Fig. 2 (A to D, G, and H), although the FEA and experiments show the same trend, there are slight discrepancies between them quantitatively. The errors introduced in manufacturing, the nonuniformity in material processing, and the noise signals in experiments can cause deviations between

simulations and experiments. Here, we use the multilayer perceptron (MLP) regression algorithm in deep learning to ensure accurate calibration of the wireless sensors (fig. S28A). The feature set involves the time-domain waveform of the nonlinear vibration and the frequency-domain waveform obtained through a fast Fourier transform (fig. S28B).

Using one cycle of damped vibration as the feature set, the sampling rate can achieve 15 Hz (i.e., actuating the micro-magnet 15 times per second; fig. S29). To mitigate the influence of noise, especially for the cases that use smaller magnets or require wireless acquisition at further distances, we exploit 16 consecutive cycles of damped vibrations as the test set (sampling rate to  $\sim 1$  Hz). The  $R^2$  of the model in this case reaches more than 95% (95.5% for viscosity, 99.89% for pressure, 98.1% for glucose concentration; fig. S30A). As shown in fig. S30 (B to D), when providing the model with a substantial volume of test data (over 1000 cycles), the MLP regression models can predict the viscosity, pressure, and glucose concentration with  $R^2$  surpassing 98%, and with detection precisions of 0.2 cP for viscosity, 1 mmHg for pressure, and 2 mM for glucose concentration. The results indicate a

trade-off between sampling rate and measurement accuracy, and the precisions of pressure and glucose concentration demonstrated here are adequate for some clinical needs (49, 50).

Furthermore, the vibration frequencies of the magnetic implants can be designed to cover a broad range (text S6 and fig. S31). As shown in fig. S32, an elastic circular membrane with a larger diameter leads to lower vibration frequencies. Optimization of the dimensions of the magnetic implants can tune their vibrations to separated frequency bands. As shown in fig. S33, a membrane (open cavity) with a thickness of 40  $\mu\text{m}$  and a diameter of 8 mm exhibits a vibration frequency of 73 Hz, while another membrane (sealed cavity) with different dimensions (thickness: 40  $\mu\text{m}$ , diameter: 6 mm) vibrates at a frequency of 100 Hz. The difference in frequency band creates possibilities for multiplexed wireless sensing using multiple magnetic implants. To eliminate the interference between adjacent micro-magnets, a distance of more than 9 mm is necessary (fig. S34) (51). As shown in Fig. 2I, the experimental demonstration of multiplexed sensing incorporates two magnetic implants, including implant 1 (sealed-cavity, membrane thickness: 40  $\mu\text{m}$ , membrane diameter: 6 mm, without surface modification) for the measurement of pressure, and implant 2 (open-cavity, membrane thickness: 40  $\mu\text{m}$ , membrane diameter: 8 mm, with surface modification) designed for sensing of glucose concentration. This configuration enables simultaneous detection of liquid pressure and glucose concentration. The activation coil and the TMR sensor from the same wearable device can excite the vibrations of the two magnetic implants and record the variations of the magnetic field. The fractional change in frequency ( $\Delta f/f_0$ ) reveals that implant 1 mainly responds to the pressure, whereas implant 2 shows a more obvious dependence on glucose concentration (Fig. 2, J and K). In addition, adopting different surface modifications to multiple magnetic implants allows for multiplex biochemical sensing. As shown in fig. S35, two magnetic implants modified with Con-A and albumin antibody respectively can operate together and selectively detect glucose and albumin. These results demonstrate the capability of magnetic implants in multiplexed wireless sensing.

### In vivo biophysical and biochemical sensing in rat models

The chip-less and battery-less nature, as well as the biocompatible encapsulation (i.e., parylene-C), ensures the biosafety of the magnetic implants. As shown in Fig. 3 (A and B), the proliferation experiment (cocultured with L929 rat fibroblast cells) on the magnetic implant shows similar results compared to the control group, indicating its minimal impact on cell proliferation. The *in vitro* cell proliferation experiments in fig. S36 indicate that MWCNTs can stably bind to the magnets without dispersing to other parts of the human body, thus minimizing any potential adverse effects on human health (52, 53). The biocompatibility makes the magnetic implants suitable for *in vivo* applications. Chronic implantation of the magnetic implants in rat brains (2 weeks:  $n = 4$ , 3 months:  $n = 2$ , control group:  $n = 1$ ) is necessary to evaluate their biosafety and biocompatibility. By using rabbit anti-Iba1 (1:500; Abcam) to label microglia and mouse anti-chondroitin sulfate (1:400; Sigma-Aldrich) to detect production of chondroitin sulfate proteoglycan, immunofluorescence test on the rat brain (2 weeks after implantation) confirms that the magnetic implants have no adverse effects on the brain tissue (Fig. 3C and figs. S37 and S38). Three months after implantation, hematoxylin and eosin (H&E) staining on multiple organs, including the brain, heart, lung, liver, spleen, and kidney, demonstrates that the implants do not trigger inflammation in the organs (Fig. 3D). The results indicate that the

elements present in the magnetic implants do not disperse or infiltrate into other organs over an extended duration of implantation. In addition, our system has a specific absorbed radiation (SAR) of 0.199 W/kg for the head, which is a safe value according to the standards of the International Commission on Non-Ionizing Radiation Protection (ICNIRP; text S7), (54). The cell viability, immunofluorescence test, H&E staining, and low SAR value together validate the biosafety of the magnetic implants, thereby proving their suitability for biomedical applications.

During the mounting of the wearable device and the insertion of the implant, the relative position between them may influence the actuation and vibration of the micro-magnet, thereby affecting the accuracy in the measurement of pressure and other parameters. One approach to addressing this issue is to use the four Hall sensors in the fully integrated wearable device for positioning the magnetic implant (fig. S39). The accuracy reaches 0.027 mm, 0.077 mm, 0.006 mm, 0.11°, and 0.13° for  $x$ ,  $y$ ,  $z$ ,  $\theta$ , and  $\varphi$ , respectively. Such small positioning errors permit accurate sensing (fig. S40, A to E). As a comparison, a shift of 0.1 mm along the  $Y$  axis only results in an error of 0.1 mmHg ( $\Delta f/f_0 = 0.032\%$ ) in pressure sensing, and a rotation of 0.1° around  $\theta$  leads to an error of 0.07 mmHg ( $\Delta f/f_0 = 0.023\%$ ; text S8 and fig. S40F). An alternative means to eliminate the influence caused by changes in relative positions is to collect vibration waveforms of the magnetic implant at different relative positions for systematic calibration. The deep learning model yields an  $R^2$  of 98.7% and a mean absolute error of 0.2 mmHg. The systematic calibration and deep learning model provide effective means for accurate sensing when the magnetic implant and wearable device are located at various relative positions. This is especially useful for *in vivo* applications because the motion from the subject may change the relative positions of the wearable device and the magnetic implant (text S9 and figs. S41 to S44).

We apply these implants to a rat brain and demonstrate the capability in wireless monitoring of CSF viscosity, ICP, and CSF glucose levels, as these parameters are important indicators for the diagnosis and treatment of traumatic brain injury (TBI), stroke, intracranial hemorrhage, acute meningitis, and brain inflammation (50, 55–58). During craniotomy, dental cement (Kerr, Dyad Flow) securely attaches the magnetic implant to the skull with a drilled hole (diameter: 5.5 mm). The micro-magnet on the membrane faces toward the CSF through the craniotomy site (Fig. 4A). The computed tomography (CT) images in Fig. 4B and fig. S45 clearly visualizes the location of the magnetic implant in the rat's brain. After suturing and cleaning the wound, the rat recovers from anesthesia and can behave normally (Fig. 4, C and D, and fig. S46). Placing the fully integrated wearable device on the rat's head enables subsequent monitoring of physical and chemical parameters in the brain (Fig. 4, E and F).

*In vivo* adjustment of viscosity exploits the fact that higher temperature leads to lower viscosity of the fluid (59). Here, a hot air gun (100°C) placed 6 cm away from the head of a rat increases the viscosity of CSF to ~45°C, thereby effectively reducing the viscosity of the fluid (Fig. 4G) (60). The wearable device mounted on the head of the rat then actuates the magnetic implant and records the intensity of the alternate magnetic field through the integrated TMR sensor. The waveform in Fig. 4H reveals that vibrations at high temperatures (i.e., lower viscosities) exhibit a noticeable slower damping compared to those at low temperatures (i.e., higher viscosities). The fitted damping factor is 232.15 before heating, gradually decreases to 165.96 during heating, and then returns to 236.35 after further cooling for ~4 s (Fig. 4, I to K).

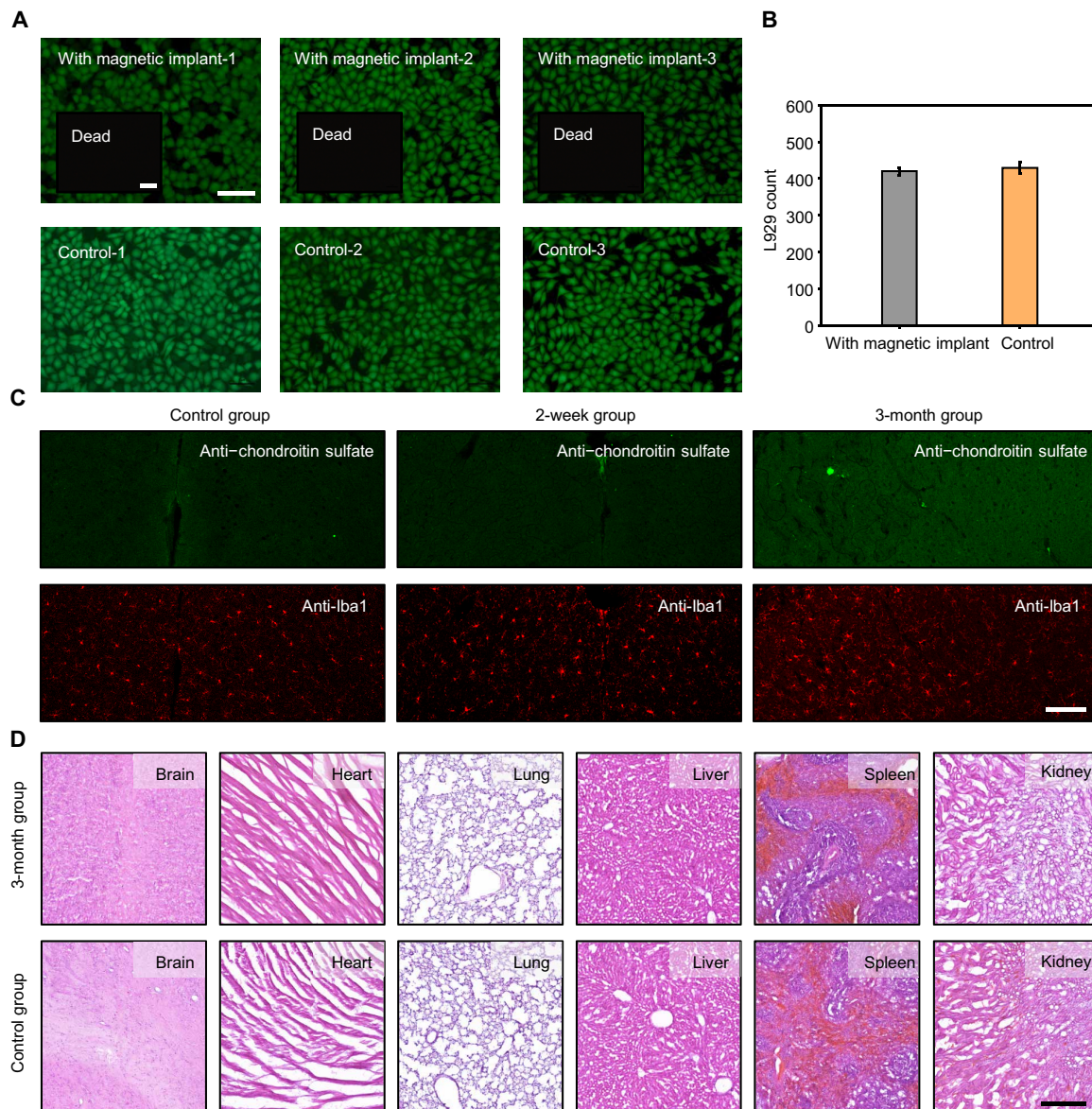


**Fig. 3. Biocompatibility of the magnetic implant.** (A) Fluorescent images of L929 rat fibroblast cells cultured on the magnetic implants for 2 weeks with calcein AM/propidium iodide. The green color (calcein AM) indicates live cells, and the red color (propidium iodide) in insets indicates dead cells. Scale bars, 5  $\mu\text{m}$ . (B) Comparison between the control group and magnetic implants in cell proliferation. Error bars correspond to the calculated SD from three measurements. (C) Immunofluorescent staining results (blue: cell nucleus; green: mouse anti-chondroitin sulfate; red: rabbit anti-Iba1) conducted on the brains of rats 2 weeks after implantation. Scale bar, 200  $\mu\text{m}$ . (D) Hematoxylin and eosin staining images of the brains, hearts, lungs, livers, spleens, and kidneys of rats with magnetic implants for 3 months. Scale bar, 200  $\mu\text{m}$ .

We carry out *in vivo* measurements of ICP in a rat model and induce variations in ICP through abdominal compression (Fig. 5A) (10). The experiment exploits a commercial pressure sensor (JR-Intellicom, JR-3100D) inserted into the brain through the craniotomy and a magnetic implant placed on top of a drilled hole in the skull (Fig. 5B and fig. S47). A close resemblance between the vibration frequency of the magnetic implant and the output of the commercial sensor indicates the accuracy and reliability of the magnetic implants in measuring abnormal sudden changes of ICP (Fig. 5C, implants: orange dots, commercial sensor: gray curve). Additional abdominal compression with various intensities (i.e.,

heavy, moderate, and light) results in different vibration frequencies of the magnetic implant. As shown in Fig. 5D and fig. S48, heavier abdominal compression leads to higher vibration frequency, indicating an elevated ICP. The magnetic implant maintains a consistent level of stability after implantation. Experiments performed on days 1 and 3 both show obvious variations of vibration frequency during abdominal compression (Fig. 5E and fig. S49). It is worth mentioning that the vibration frequency exhibits a shift on day 3, due to the possibility of the attachment of biofilms, the penetration of biofluids, and other complex *in vivo* conditions. To guarantee accurate measurement, a calibration is necessary every few

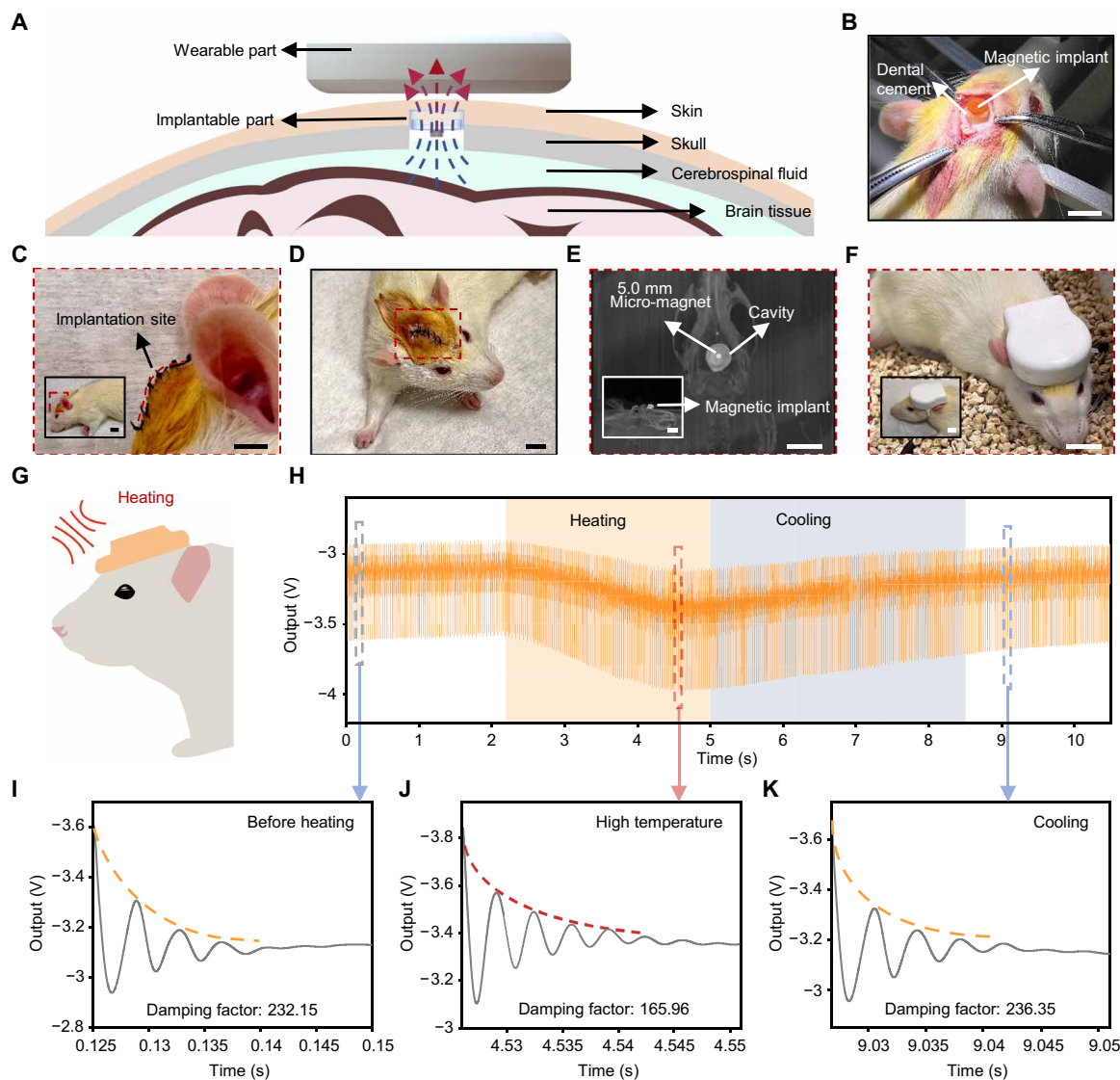


**Fig. 4. In vivo wireless sensing of CSF viscosity from the damping factor in rat's brain.** (A) Schematic illustration of the in vivo wireless measurement in rat's brain. (B) Computed tomography (CT) image (top view) of the magnetic implant in the brain of a rat. The inset shows the side view CT image. Scale bars, 1 cm. (C) Optical image of a rat with a fully sutured scalp after surgery. The inset is an optical image with a larger field of view. Scale bars, 5 mm. (D) Optical image of a freely moving rat after surgery. Scale bar, 5 mm. (E) CT image (top view) of the magnetic implant in the brain of a rat. The inset shows the side view CT image. Scale bars, 1 cm. (F) Optical image of a rat with a mounted wearable device. Scale bars, 1 cm. (G) Schematic diagram of altering CSF viscosity through heating. (H) Waveform captured from the wearable device during the actuation and damped vibration of the magnetic implant under different temperatures. (I to K) Magnified views of the damped vibration before heating (I), during heating (J), and after cooling (K).

days. Using a larger magnet to produce stronger actuation and adding anticoagulant or hydrophobic coatings (61) represent alternative means to potentially mitigate the signal drift. As demonstrations of the long-term operation and the signal drift of magnetic implants, text S10 and fig. S50 illustrate the anticoagulant coating of phosphatidylcholine to the magnetic implant, and corresponding in vivo measurements in a rat model for 7 days; fig. S51 shows the 12-day in vivo measurements from a larger magnetic implant (total diameter: 8 mm, diameter of the magnet: 2.5 mm, height of the magnet: 1 mm).

As illustrated in Fig. 5 (F and G), in vivo measurement of biochemicals, such as glucose concentration in CSF, demands an additional craniotomy site (diameter: 1 mm) on the skull located above the implantation site of the open-cavity magnetic implant. Injection

of glucose solution through this site enables adjustment of glucose level in the CSF. Here, the injected solution with a small volume (100  $\mu$ l) and a high concentration (1 M) can diffuse glucose into the CSF. The Con-A–modified MWCNTs on the micro-magnet surface gradually absorb the glucose in the CSF, thereby increasing the mass of the membrane and the detected vibration frequency (Fig. 5, H and I). The processes of diffusion and absorption cover a period of ~40 min, during which the vibration frequency of the magnetic implant decreases from 93.83 to 72.88 Hz (Fig. 5J). Since the desorption of glucose molecules and Con-A–modified MWCNTs is slow, a limitation of the current system is that it cannot accurately reflect the decrease in glucose concentration (62, 63). However, in some specific clinical scenarios, such as the recovery process of TBI, the

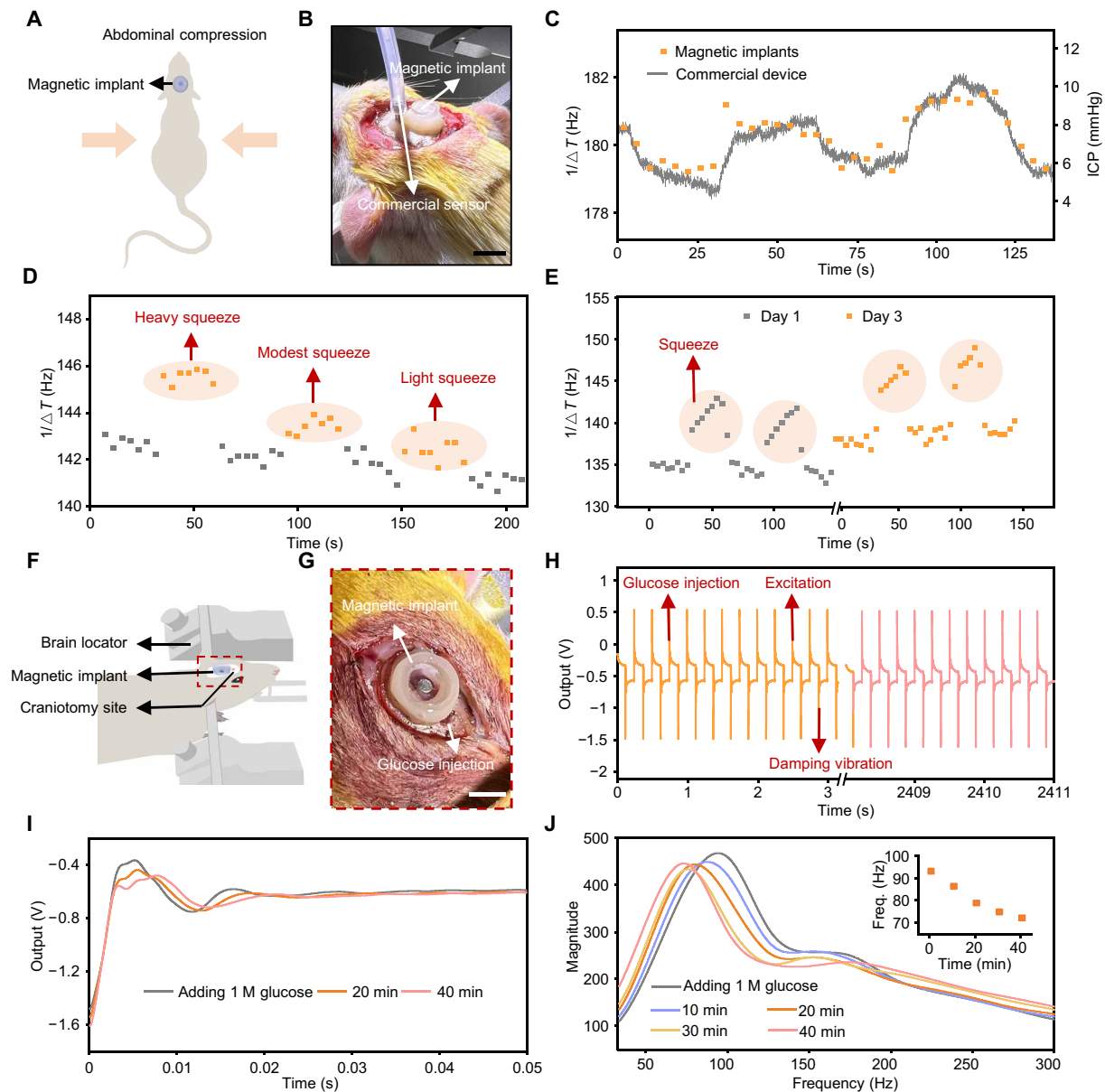


**Fig. 5. In vivo wireless sensing of ICP and CSF glucose level from the vibration frequency.** (A) Schematic illustration of abdominal compression to adjust ICP. (B) Optical image showing the simultaneous measurement of ICP using the magnetic implant and a commercial pressure sensor. Scale bar, 1 cm. (C) Fluctuations of ICP captured from the magnetic implant (orange dots) and the commercial pressure sensor (gray curve) during abdominal compression. (D) Response of the magnetic implant under abdominal compression with various intensities. (E) Response of the magnetic implant during abdominal compressing on days 1 and 3. Data points inside the light orange ellipses correspond to the ICP during squeezing. (F and G) Schematic illustration (F) and optical image (G) of the experimental setup for altering intracranial glucose concentration in rats. Scale bar, 5 mm. (H) Waveform captured from the wearable device during the process of glucose diffusion in CSF. (I) Magnified views of the one-cycle vibration waveforms over time after glucose injection. (J) FFT results from the vibration of the magnetic implant under different glucose levels. The inset shows the peak frequency in FFT as a function of time, indicating the diffusion of glucose across the CSF over time.

concentration of glucose in the CSF gradually increases, which can be detected by the magnetic implant.

## DISCUSSION

The chip-less, battery-less magnetic implants reported here can pair with a fully integrated wearable device to enable wireless monitoring of biophysical and biochemical parameters within the body, such as

viscosity, pressure, and glucose concentration. This system (i.e., the magnetic implant paired with the wearable device) offers qualitatively differentiated capabilities compared with existing wireless implantable sensors. First, the wearable device establishes a bidirectional interaction with the implant through a magnetic field. This mechanism eliminates commercial chips, batteries, and/or coils in the implants and does not require bulky readout equipment, thereby reducing the overall dimensions of the system for monitoring to underpin

pervasive healthcare. Second, the implants incorporate soft materials to generate vibration amplitudes two orders of magnitude larger than those of conventional MEMS, with tailorable vibration frequencies. Such designs facilitate the measurements in an unshielded environment and provide possibilities in multiplexed sensing using different frequency bands. Third, the vibration features of the magnetic implants after surface modification not only reflect their surrounding physical conditions but also involve information on the concentration of a specific chemical. A deep learning model correlates the time-domain and frequency-domain data with various physical and chemical parameters and makes the measurement insensitive to the relative positions between the magnetic implant and the wearable device. Fourth, the chip-less and battery-less nature of the implant promotes long-term biosafety, thereby supporting *in vivo* applications. Experiments in rat models validate the capabilities in wireless monitoring of CSF viscosity, ICP, and CSF glucose levels, offering personalized and customized references for the treatment of brain diseases, and the assessment of brain function and injuries. These advancements highlight our system as a complementary technology to existing wireless sensing modalities, serving as a unique tool for quantitative, continuous monitoring of a diverse set of biophysical and biochemical conditions.

Although the *in vivo* applications demonstrated here focus on the brain, the wireless sensing system can serve as an efficient diagnostic tool for many other regions inside the body in diverse application scenarios, including blood pressure and viscosity in the cardiovascular system, contact force in dentistry and orthopedics, pressure in the abdominal region, as well as the distributions and concentrations of proteins, peptides, small molecules, and cells in various regions inside the human body. Monitoring of these conditions outside of hospital settings is useful for the diagnosis, treatment, and management of a variety of acute and chronic diseases, such as traumatic injuries, heart failure, diabetes, cancer, liver cirrhosis, ascites, and others. Many opportunities lie in the development of wireless biosensors by incorporating functional surface modifications (e.g., antibody and aptamer) into the magnetic implant. The resulting miniaturized system will allow for continuous sensing of a broader range of chemicals and biomolecules, all in a wireless manner. In addition, downsizing the magnetic implants for minimally invasive insertion, increasing the distance of wireless actuation and recording to target deep tissues, and leveraging the frequency band for multiplexed, multimodal sensing represent other important areas for future developments. Meanwhile, long-term stability remains a challenge for magnetic implants since the attachment of biofilms and the penetration of biofluids can cause signal drift and device failure. Incorporating anticoagulant coating and highly stable polymers (64–66) into the magnetic implants represents possible solutions to enable chronic, accurate measurement. These advancements will enhance the relevance and impact of our system in healthcare applications and may renovate the diagnosis and treatment of a series of diseases.

## MATERIALS AND METHODS

### Circuit design of the wearable device

The wearable device comprised a TMR sensor (TMR9002CP, Doway-Tech) with high sensitivity, a Bluetooth SoC (nrF52832, Nordic), a copper coil (1000 turns, Chuangli), an excitation circuit, four Hall sensors (BMM150, Bosch), and a lithium-ion battery (1200 mA, JieXun). The Bluetooth module, copper coil, and other components

were powered directly by the lithium-ion battery with a voltage of 7.4 V. The excitation circuit used a DC-DC converter (TPS61170DRVR, Texas Instruments) to boost the voltage to 15 V. The Bluetooth SoC controlled the optocoupler switch (TLP187, Toshiba) within the excitation circuit, generating a square wave voltage input to the coil with a frequency of 4 Hz and a peak value of 15 V. This alternate voltage generated a square wave magnetic field that periodically attracted and released the magnet. The four Hall sensors estimated the initial position of the magnet on the membrane, while the TMR sensor captured the vibration signal of the micro-magnet. The analog output from the TMR sensor was then digitized by ADC and transmitted to a mobile terminal through Bluetooth. Subsequent signal processing extracted information related to the liquid viscosity, pressure, and glucose concentration.

### Fabrication of the PDMS cavity

Fabrication of the PDMS (Sylgard 184, Dow Corning) cavity started with the mixing of the base and curing agent of PDMS at a weight ratio of 10:1. The sealed cavity was a trilayer structure in PDMS, including a bottom substrate (thickness: 1 mm), a middle ring (thickness: 1 mm), and a top circular membrane (thickness: 40  $\mu\text{m}$ ). The open cavity in PDMS was a bilayer structure, including a middle ring layer (thickness: 1 mm) and a top circular membrane (thickness: 40  $\mu\text{m}$ ). Laser cutting defined the patterns of each layer, and uncured PDMS bonded three layers together to form a sealed cavity after heating at 80°C for 40 min. A cylindrical magnet (D1001A-10, SuperMagneticMan) in neodymium iron boron with a diameter of 1.5 mm and a height of 0.8 mm coated with parylene-C layer (thickness: 10  $\mu\text{m}$ ) promoted the biocompatibility of the magnetic implants. Uncured PDMS enabled the bonding of the magnet to the center of the top membrane layer. Heating at 80°C for 40 min cured the PDMS and completed the process.

### Laser cutting of PDMS with CO<sub>2</sub> laser

A continuous wave CO<sub>2</sub> laser (VLS3.60DT Platform-SYS, Universal Laser Systems Inc.) can cut PDMS into various designed patterns. The wavelength, power, and cutting speed together determined the processing effect. The full power of the laser machine was 30 W, the maximum speed was 1.27 m/s, and the points per inch (PPI) was 1000. Here, cutting a 40- $\mu\text{m}$ -thick PDMS required 20% of the full power, 9% of the maximum speed, and a PPI of 1000. Cutting a 1-mm-thick PDMS required 20% of the full power, 2% of the maximum speed, and a PPI of 1000.

### Fabrication of the vertical dense array of MWCNTs

The fabrication process involved growing a SiO<sub>2</sub> buffer layer (thickness: 1  $\mu\text{m}$ ) on the Si substrate through thermal oxidation. This buffer layer prevented the direct fusion of the metal catalyst to the Si substrate. Following that, a thin layer of Fe (thickness: 2 nm), deposited through electron beam evaporation, served as the catalyst layer for MWCNTs growth. A quartz boat held the sample inside a reaction chamber, pumped to a pressure below  $\sim 1.5 \times 10^{-2}$  torr. After introducing and stabilizing argon (Ar) gas at a flow rate of 7 sccm and hydrogen (H<sub>2</sub>) gas at a flow rate of 3 sccm, the pressure inside the chamber settled to be  $\sim 0.36$  torr. The heating zone's temperature gradually increased to 700°C at a rate of 9.5°C/min. Upon reaching a temperature of 695°C, the radio frequency (RF) power supply switched on, setting the actual power to 250 W. After achieving a normal glow discharge inside the quartz tube, methane at a flow rate of

approximately 14.7 sccm entered the chamber until the chamber pressure reached around 0.936 torr, which initiated the growth of MWCNTs. The height of the MWCNTs had a positive relationship to the duration of the growth process. Once the designated growth process was over, the RF power supply was switched off. The flow of methane and hydrogen stopped and the equipment started to cool down. A flow of 3.5 sccm of argon was maintained to expedite the cooling process. When the temperature dropped to 100°C, the gas flow all stopped terminating the growth process.

### Transfer of MWCNTs from Si wafer to PDMS

The sample of MWCNTs (height: 50  $\mu\text{m}$ ) was on a Si wafer, with a thin layer of Fe (thickness: 2 nm) in between. The fabrication started with the spin-coating and curing process (80°C for 40 min) of the first PDMS layer (thickness: 20.0  $\mu\text{m}$ ) on a polyethylene terephthalate film. Then, the uncured second PDMS layer (thickness: 20  $\mu\text{m}$ ) spin-coated on the first PDMS layer trapped the MWCNTs on the wafer. After curing the second PDMS layer at 80°C for 40 min, it firmly held the MWCNTs to allow for the release from the Si wafer. Laser cutting patterned the PDMS membrane with MWCNTs into a circular shape with a diameter of 1.5 mm.

### Modification of MWCNTs with Con-A

The modification began with immersing the membrane in PBSE (3 mg/ml; Xianding Bio-Technology Co., Ltd) solution in *N,N'*-dimethylformamide (DMF; CONCORD Technology) for 4 hours. Then, immersing the membrane with DMF and phosphate-buffered solution (PBS), and soaking it in PBS (SinoDetech) containing 1 mM calcium ions, 1 mM manganese ions, and Con-A (3 mg/ml; Shanghai Yuanye Bio-Technology Co., Ltd) for 30 min completed the binding process. After washing away the excess Con-A with PBS, immersing in a 0.1% ethanolamine (Energy Chemical) aqueous solution for 1 hour blocked unbound Con-A binding sites. Subsequently, immersing the sample in a 0.1% Tween 20 (Coolaber) solution for 30 min blocked exposed MWCNTs and reduced nonspecific binding. Last, washing the membrane with PBS completed the specific modification of MWCNTs for the selective binding with glucose molecules. The resulting membrane was suitable for glucose-sensing applications.

### Modification of MWCNTs with albumin antibody and human IgG antibody

The modification began with immersing the membrane with MWCNTs in PBSE (3 mg/ml; Xianding Bio-Technology Co., Ltd) solution in pure methanol for 1 hour at room temperature. Then, after rinsing with pure methanol to wash away excess reagent, the membrane with MWCNTs required an overnight incubation in PBS with albumin antibody (3 mg/ml; Proteintech) or human IgG antibody (3 mg/ml; goat anti-human IgG, Wuxi NEST Biotechnology Co., Ltd). Following the incubation, additional steps involved rinsing in deionized water for 6 hours and drying. Last, incubation in 0.1% ethanolamine (Energy Chemical) aqueous solution for 1 hour and immersing in 0.1% Tween 20 (Coolaber) solution for 30 min blocked the unbound Con-A binding sites and MWCNTs.

### Testing environment

#### Viscosity

Different ratios of glycerol-water solutions had distinct viscosities. During the test, the magnetic implants were located in a liquid

environment with various viscosities. The wearable device positioned above the magnetic implants collected the signals resulting from changes in the magnetic field caused by the vibration of the micro-magnet. The damping of the vibration depended on the liquid viscosity.

#### Pressure

The pressure at the lower end of the customized U-tube had a positive relationship with the liquid (artificial CSF, MREDA) height difference between the two pipes. Positioned above the magnetic implant at the lower end, the wearable device collected the signals resulting from changes in the magnetic field caused by the vibration of the micro-magnet. The vibration frequency depended on the liquid pressure.

#### Glucose concentration

The MWCNTs-PDMS membrane, modified with Con-A, adhered to the micro-magnet using uncured Ecoflex Gel. Curing at room temperature for 10 min promoted the adhesion between the MWCNTs-PDMS membrane and the micro-magnet. Then, fixing the open-cavity implants with MWCNTs-PDMS membrane into the liquid environment (artificial CSF) with different concentrations of glucose, the wearable device positioned below the open-cavity implants can collect the signals resulting from changes in the magnetic field caused by the vibration of the magnet. The vibration frequency depended on the concentration of glucose.

### Automated calibration at different relative positions

During calibration, the magnetic implants are located in a liquid environment (artificial CSF) with a fixed position. A customized four-axis automated displacement platform held the wearable device. The platform moved along the X, Y, and Z axes and rotated around the X axis to adjust the relative position between the wearable device and the magnetic implant. In each position, the wearable device actuated the magnetic implant and recorded the intensity of the alternate magnetic field. The recorded signals served as training samples in deep learning.

### Deep learning model

A PowerLab computer interface (Model 16/35, ADInstruments) collected the signal at a frequency of 200 kHz. A peak detection algorithm enabled the extraction of the vibration signal. The time-domain and frequency-domain data served as features for deep learning. The actual values of viscosity, pressure, and glucose concentration were truth values in the deep learning model. The vibration signals for calibration of viscosity, pressure, and glucose concentration in the benchtop test were training samples. The preprocessed signals from the in vivo test were testing samples. The MLP regression algorithm allowed for reliable regression of the variables (e.g., viscosity, pressure, and glucose concentration) from the testing samples.

### In vitro cytotoxicity evaluation

The proliferation experiment began with soaking the magnetic implants in 75% alcohol, disinfecting them with ultraviolet light irradiation, and washing them with PBS three times. Then, the preparation of L929 cells involved seeding the cells in 96-well plates at a density of 5000 per well along with the magnetic implants. The control group used RPMI 1640 basal medium with 10% fetal bovine serum. After 3 days of incubation, Calcein AM/propidium iodide (Biyuntian Co, Ltd.) staining was carried out, with green (calcein AM) for live cells and red (propidium iodide) for dead cells. The fluorescence images were obtained with fluorescence microscopy (ZEISS Axiovert).

## Surgical procedures

All procedures associated with animal studies followed recommendations with the ethical guidelines of the Institutional Animal Center Peking University. The Institutional Animal Care and Use Committee (IACUC) at Peking University (Protocol No. FT-HanMD-1) approved the protocol. Male rats (SD, age at initiation of the treatment: at least 9 weeks, but no more than 15 weeks, purchased from Beijing Vitalstar Biotechnology Co., Ltd.) were acclimated up to 5 days before surgery. Animals were anesthetized using isoflurane gas during the implantation surgery and measurement. Surgical procedures removed the furs on the head and created a craniotomy (5.5-mm diameter) in the skull located in the parietal lobe area. Next, we carefully cut the dura mater and introduced saline into the craniotomy to establish a liquid environment for testing purposes. After cleaning the implantation site and the surface of the magnetic implant, dental cement enabled the bonding of the magnetic implant to the designated site of the skull. Disinfecting and suturing the wound completed the implantation surgery, followed by administering penicillin for anti-inflammatory effects and injection of meloxicam for pain relief. Closing the scalp completely sealed the magnetic implant inside, without any transcutaneous wires. Placing the wearable device on the head of the rat enabled wireless actuation of the magnetic implant and wireless recording of the dynamic magnetic field.

## In vivo biocompatibility test

All procedures associated with animal studies followed recommendations with the ethical guidelines of the Institutional Animal Center Peking University. The IACUC at Peking University (Protocol No. FT-HanMD-1) approved the protocol. After the 2-week and 3-month monitoring window, rats implanted with magnetic implants (2 weeks:  $n = 4$ ; 3 months:  $n = 2$ ) and a rat without implantation (control group,  $n = 1$ ) were dissected through a surgical operation, removing organs including the brain, heart, lung, liver, spleen, and kidney for histological investigations. Subsequently, organs went through 1-week fixing in polyoxymethylene and 5-week dehydration in sucrose solution. Then, the sliced samples of the brain tissue were stained by rabbit anti-Iba1 (1:500; Abcam) to label microglia, mouse anti-chondroitin sulfate (1:400; Sigma-Aldrich) to detect the production of chondroitin sulfate proteoglycan. In the meanwhile, organ slices from the brain, heart, lung, liver, spleen, and kidney went through H&E staining. After staining, all the samples were examined under a digital slide scanning system (PANNORAMIC SCAN, 3DHISTECH).

## In vivo biophysical and biochemical sensing on rat models

The experiments were conducted in accordance with the ethical guidelines of the Institutional Animal Center Peking University and with the approval of the IACUC of the Peking University in Beijing (Protocol No. FT-HanMD-1). Localized heating of the brain through a hot air gun (OLT8586, Oulitai) altered the viscosity of the CSF. Abdominal compression applied gentle pressure to the abdomen of the rat, resulting in a change of ICP. To adjust the glucose concentration in the CSF, the procedure introduced a high-concentration glucose solution (100  $\mu$ l, 1 M) into the craniotomy site. The frequency and damping rate of the vibration signals provided information related to CSF viscosity, ICP, and CSF glucose level. In addition, a commercial pressure sensor (JR-3100D, JR-Intellicom) inserted into the brain from a flexible tube in polyethylene (diameter: 1 mm) allowed for calibration purposes. In all the in vivo experiments, dental cement sealed the hole in

the skull and fixed the interface between the sensor and the skull to ensure secure and reliable connections.

## Supplementary Materials

### This PDF file includes:

Text S1 to S10  
Figs. S1 to S51  
Legends for movies S1 to S4  
References

### Other Supplementary Material for this manuscript includes the following:

Movies S1 to S4

## REFERENCES AND NOTES

- R. Feiner, T. Dvir, Tissue–electronics interfaces: From implantable devices to engineered tissues. *Nat. Rev. Mater.* **3**, 17076 (2018).
- M. H. Yacoub, C. McLeod, The expanding role of implantable devices to monitor heart failure and pulmonary hypertension. *Nat. Rev. Mater.* **15**, 770–779 (2018).
- W. Bai, J. Shin, R. Fu, I. Kandela, D. Lu, X. Ni, Y. Park, Z. Liu, T. Hang, D. Wu, Y. Liu, C. R. Haney, I. Stepien, Q. Yang, J. Zhao, K. R. Nandoliya, H. Zhang, X. Sheng, L. Yin, K. MacRenaris, A. Brikha, F. Aird, M. Pezhouh, J. Hornick, W. Zhou, J. A. Rogers, Bioresorbable photonic devices for the spectroscopic characterization of physiological status and neural activity. *Nat. Biomed. Eng.* **3**, 644–654 (2019).
- B. J. Nelson, I. K. Kaliakatsos, J. J. Abbott, Microrobots for minimally invasive medicine. *Annu. Rev. Biomed. Eng.* **12**, 55–85 (2010).
- W. T. Abraham, L. W. Stevenson, R. C. Bourge, J. A. Lindenfeld, J. G. Bauman, P. B. Adamson, Sustained efficacy of pulmonary artery pressure to guide adjustment of chronic heart failure therapy: Complete follow-up results from the CHAMPION randomised trial. *Lancet* **387**, 453–461 (2016).
- S. K. Garg, D. Liljenquist, B. Bode, M. P. Christiansen, T. S. Bailey, R. L. Brazg, D. S. Denham, A. R. Chang, H. K. Akturk, A. Dehennis, K. S. Tweden, Evaluation of accuracy and safety of the next-generation up to 180-day long-term implantable Eversense continuous glucose monitoring system: The PROMISE study. *Diabetes Technol. Ther.* **24**, 84–92 (2022).
- H. Lorach, A. Galvez, V. Spagnolo, F. Martel, S. Karakas, N. Interling, M. Vat, O. Favier, C. Harte, S. Komi, J. Ravier, T. Collin, L. Coquoz, I. Sakr, E. Baaklini, S. D. Hernandez-Charpak, G. Dumont, R. Buschman, N. Buse, T. Denison, I. van Nes, L. Asboth, A. Watrin, L. Struber, F. Sauter-Starace, L. Langar, V. Auboiroux, S. Carda, S. Chabardes, T. Aksenova, R. Demesmaeker, G. Charvet, J. Bloch, G. Courtine, Walking naturally after spinal cord injury using a brain–spine interface. *Nature* **618**, 126–133 (2023).
- C.-H. Chiang, S. M. Won, A. L. Orsborn, K. J. Yu, M. Trumpis, B. Bent, C. Wang, Y. Xue, S. Min, V. Woods, C. Yu, B. H. Kim, S. B. Kim, R. Huq, J. Li, K. J. Seo, F. Vitale, A. Richardson, H. Fang, Y. Huang, K. Shepard, B. Pesaran, J. A. Rogers, J. Vivoti, Development of a neural interface for high-definition, long-term recording in rodents and nonhuman primates. *Sci. Transl. Med.* **12**, eaay4682 (2020).
- T. J. Oxley, N. L. Opie, S. E. John, G. S. Rind, S. M. Ronayne, T. L. Wheeler, J. W. Judy, A. J. McDonald, A. Dornom, T. J. H. Lovell, C. Steward, D. J. Garrett, B. A. Moffat, E. H. Lui, N. Yassi, B. C. V. Campbell, Y. T. Wong, K. E. Fox, E. S. Nurse, I. E. Bennett, S. H. Bauquier, K. A. Liyanage, N. R. van der Nagel, P. Perucca, A. Ahnood, K. P. Gill, B. Yan, L. Churilov, C. R. French, P. M. Desmond, M. K. Horne, L. Kiers, S. Praver, S. M. Davis, A. N. Burkitt, P. J. Mitchell, D. B. Grayden, C. N. May, T. J. O'Brien, Minimally invasive endovascular stent-electrode array for high-fidelity, chronic recordings of cortical neural activity. *Nat. Biotechnol.* **34**, 320–327 (2016).
- S.-K. Kang, R. K. J. Murphy, S.-W. Hwang, S. M. Lee, D. V. Harburg, N. A. Krueger, J. Shin, P. Gamble, H. Cheng, S. Yu, Z. Liu, J. G. McCall, M. Stephen, H. Ying, J. Kim, G. Park, R. C. Webb, C. H. Lee, S. Chung, D. S. Wie, A. D. Gujar, B. Vemulapalli, A. H. Kim, K.-M. Lee, J. Cheng, Y. Huang, S. H. Lee, P. V. Braun, W. Z. Ray, J. A. Rogers, Bioresorbable silicon electronic sensors for the brain. *Nature* **530**, 71–76 (2016).
- P. G. Saiz, R. Fernández de Luis, A. Lasheras, M. I. Arriortua, A. C. Lopes, Magnetoelastic resonance sensors: Principles, applications, and perspectives. *ACS Sens.* **7**, 1248–1268 (2022).
- Z. Liu, Y. Ma, H. Ouyang, B. Shi, N. Li, D. Jiang, F. Xie, D. Qu, Y. Zou, Y. Huang, H. Li, C. Zhao, P. Tan, M. Yu, Y. Fan, H. Zhang, Z. Wang, Z. Li, Transcatheter self-powered ultrasensitive endocardial pressure sensor. *Adv. Funct. Mater.* **29**, 1807560 (2019).
- X. Yu, H. Wang, X. Ning, R. Sun, H. Albadawi, M. Salomao, A. C. Silva, Y. Yu, L. Tian, A. Koh, C. M. Lee, A. Chempakasseril, P. Tian, M. Pharr, J. Yuan, Y. Huang, R. Oklu, J. A. Rogers, Needle-shaped ultrathin piezoelectric microsystem for guided tissue targeting via mechanical sensing. *Nat. Biomed. Eng.* **2**, 165–172 (2018).
- J. Li, Y. Liu, L. Yuan, B. Zhang, E. S. Bishop, K. Wang, J. Tang, Y.-Q. Zheng, W. Xu, S. Niu, L. Beker, T. L. Li, G. Chen, M. Diyaolu, A.-L. Thomas, V. Mottini, J. B. H. Tok, J. C. Y. Dunn,

- B. Cui, S. P. Paşca, Y. Cui, A. Habtezion, X. Chen, Z. Bao, A tissue-like neurotransmitter sensor for the brain and gut. *Nature* **606**, 94–101 (2022).
15. J.-W. Seo, K. Fu, S. Correa, M. Eisenstein, E. A. Appel, H. T. Soh, Real-time monitoring of drug pharmacokinetics within tumor tissue in live animals. *Sci. Adv.* **8**, eabk2901 (2022).
  16. L. Lu, P. Gutruf, L. Xia, D. L. Bhatti, X. Wang, A. Vazquez-Guardado, X. Ning, X. Shen, T. Sang, R. Ma, G. Pakeltis, G. Sobczak, H. Zhang, D.-O. Seo, M. Xue, L. Yin, D. Chanda, X. Sheng, M. R. Bruchas, J. A. Rogers, Wireless optoelectronic photometers for monitoring neuronal dynamics in the deep brain. *Proc. Natl. Acad. Sci. U.S.A.* **115**, E1374–E1383 (2018).
  17. P. J. Kennel, H. Rosenblum, K. M. Axsom, S. Alishetti, M. Brener, E. Horn, A. J. Kirtane, E. Lin, J. M. Griffin, M. S. Maurer, D. Burkhoff, G. Sayer, N. Uriel, Remote cardiac monitoring in patients with heart failure: A review. *JAMA Cardiol.* **7**, 556–564 (2022).
  18. S. Weisdorf, J. Duun-Henriksen, M. J. Kjeldsen, F. R. Poulsen, S. W. Gangstad, T. W. Kjær, Ultra-long-term subcutaneous home monitoring of epilepsy—490 days of EEG from nine patients. *Epilepsia* **60**, 2204–2214 (2019).
  19. H. C. Koydemir, A. Ozcan, Wearable and implantable sensors for biomedical applications. *Annu. Rev. Anal. Chem.* **11**, 127–146 (2018).
  20. G.-H. Lee, H. Moon, H. Kim, G. H. Lee, W. Kwon, S. Yoo, D. Myung, S. H. Yun, Z. Bao, S. K. Hahn, Multifunctional materials for implantable and wearable photonic healthcare devices. *Nat. Rev. Mater.* **5**, 149–165 (2020).
  21. M. Han, L. Chen, K. Aras, C. Liang, X. Chen, H. Zhao, K. Li, N. R. Faye, B. Sun, J.-H. Kim, W. Bai, Q. Yang, Y. Ma, W. Lu, E. Song, J. M. Baek, Y. Lee, C. Liu, J. B. Model, G. Yang, R. Ghaffari, Y. Huang, I. R. Efimov, J. A. Rogers, Catheter-integrated soft multilayer electronic arrays for multiplexed sensing and actuation during cardiac surgery. *Nat. Biomed. Eng.* **4**, 997–1009 (2020).
  22. S. Park, S. W. Heo, W. Lee, D. Inoue, Z. Jiang, K. Yu, H. Jinno, D. Hashizume, M. Sekino, T. Yokota, K. Fukuda, K. Tajima, T. Someya, Self-powered ultra-flexible electronics via nano-grating-patterned organic photovoltaics. *Nature* **561**, 516–521 (2018).
  23. S. Choi, S. I. Han, D. Jung, H. J. Hwang, C. Lim, S. Bae, O. K. Park, C. M. Tschabrunn, M. Lee, S. Y. Bae, J. W. Yu, J. H. Ryu, S.-W. Lee, K. Park, P. M. Kang, W. B. Lee, R. Nezafat, T. Hyeon, D.-H. Kim, Highly conductive, stretchable and biocompatible Ag–Au core–sheath nanowire composite for wearable and implantable bioelectronics. *Nat. Nanotechnol.* **13**, 1048–1056 (2018).
  24. K. Sim, F. Ershad, Y. Zhang, P. Yang, H. Shim, Z. Rao, Y. Lu, A. Thukral, A. Elgalad, Y. Xi, B. Tian, D. A. Taylor, C. Yu, An epicardial bioelectronic patch made from soft rubbery materials and capable of spatiotemporal mapping of electrophysiological activity. *Nat. Electron.* **3**, 775–784 (2020).
  25. E. Elmistekawy, Safety of temporary pacemaker wires. *Asian Cardiovasc. Thorac. Ann.* **27**, 341–346 (2019).
  26. J. Li, J. Liu, Z. Wu, X. Shang, Y. Li, W. Huo, X. Huang, Fully printed and self-compensated bioresorbable electrochemical devices based on galvanic coupling for continuous glucose monitoring. *Sci. Adv.* **9**, eadi3839 (2023).
  27. B. Gleich, I. Schmale, T. Nielsen, J. Rahmer, Miniature magneto-mechanical resonators for wireless tracking and sensing. *Science* **380**, 966–971 (2023).
  28. K. Kwon, J. U. Kim, S. M. Won, J. Zhao, R. Avila, H. Wang, K. S. Chun, H. Jang, K. H. Lee, J.-H. Kim, S. Yoo, Y. J. Kang, J. Kim, J. Lim, Y. Park, W. Lu, T.-I. Kim, A. Banks, Y. Huang, J. A. Rogers, A battery-less wireless implant for the continuous monitoring of vascular pressure, flow rate and temperature. *Nat. Biomed. Eng.* **7**, 1215–1228 (2023).
  29. M. E. Inda-Webb, M. Jimenez, Q. Liu, N. V. Phan, J. Ahn, C. Steiger, A. Wentworth, A. Riaz, T. Zirtiloglu, K. Wong, K. Ishida, N. Fabian, J. Jenkins, J. Kuosmanen, W. Madani, R. McNally, Y. Lai, A. Hayward, M. Mimeo, P. Nadeau, A. P. Chandrakasan, G. Traverso, R. T. Yazicigil, T. K. Lu, Sub-1.4 cm<sup>3</sup> capsule for detecting labile inflammatory biomarkers in situ. *Nature* **620**, 386–392 (2023).
  30. R. Li, H. Qi, Y. Ma, Y. Deng, S. Liu, Y. Jie, J. Jing, J. He, X. Zhang, L. Wheatley, C. Huang, X. Sheng, M. Zhang, L. Yin, A flexible and physically transient electrochemical sensor for real-time wireless nitric oxide monitoring. *Nat. Commun.* **11**, 3207 (2020).
  31. W. S. Skinner, S. Zhang, R. E. Guldberg, K. G. Ong, Magnetoelastic sensor optimization for improving mass monitoring. *Sensors* **22**, 827 (2022).
  32. C. M. Boutry, L. Beker, Y. Kaizawa, C. Vassos, H. Tran, A. C. Hinckley, R. Pfattner, S. Niu, J. Li, J. Claverie, Z. Wang, J. Chang, P. M. Fox, Z. Bao, Biodegradable and flexible arterial-pulse sensor for the wireless monitoring of blood flow. *Nat. Biomed. Eng.* **3**, 47–57 (2019).
  33. D. Seo, R. M. Neely, K. Shen, U. Singhal, E. Alon, J. M. Rabaey, J. M. Carmena, M. M. Maharbiz, Wireless recording in the peripheral nervous system with ultrasonic neural dust. *Neuron* **91**, 529–539 (2016).
  34. W. Ouyang, W. Lu, Y. Zhang, Y. Liu, J. U. Kim, H. Shen, Y. Wu, H. Luan, K. Kilner, S. P. Lee, Y. Lu, Y. Yang, J. Wang, Y. Yu, A. J. Wegener, J. A. Moreno, Z. Xie, Y. Wu, S. M. Won, K. Kwon, C. Wu, W. Bai, H. Guo, T.-L. Liu, H. Bai, G. Monti, J. Zhu, S. R. Madhupathy, J. Trueb, M. Stanslaski, E. M. Higbee-Dempsey, I. Stepien, N. Ghoreishi-Haack, C. R. Haney, T.-I. Kim, Y. Huang, R. Ghaffari, A. R. Banks, T. C. Jhou, C. H. Good, J. A. Rogers, A wireless and battery-less implant for multimodal closed-loop neuromodulation in small animals. *Nat. Biomed. Eng.* **7**, 1252–1269 (2023).
  35. Y. Kim, J. M. Suh, J. Shin, Y. Liu, H. Yeon, K. Qiao, H. S. Kum, C. Kim, H. E. Lee, C. Choi, H. Kim, D. Lee, J. Lee, J.-H. Kang, B.-I. Park, S. Kang, J. Kim, S. Kim, J. A. Perozek, K. Wang, Y. Park, K. Kishen, L. Kong, T. Palacios, J. Park, M.-C. Park, H.-J. Kim, Y. S. Lee, K. Lee, S.-H. Bae, W. Kong, J. Han, J. Kim, Chip-less wireless electronic skins by remote epitaxial freestanding compound semiconductors. *Science* **377**, 859–864 (2022).
  36. M. Lin, Z. Zhang, X. Gao, Y. Bian, R. S. Wu, G. Park, Z. Lou, Z. Zhang, X. Xu, X. Chen, A. Kang, X. Yang, W. Yue, L. Yin, C. Wang, B. Qi, S. Zhou, H. Hu, H. Huang, M. Li, Y. Gu, J. Mu, A. Yang, A. Yaghi, Y. Chen, Y. Lei, C. Lu, R. Wang, J. Wang, S. Xiang, E. B. Kistler, N. Vasconcelos, S. Xu, A fully integrated wearable ultrasound system to monitor deep tissues in moving subjects. *Nat. Biotechnol.* **10.1038/s41587-023-01800-0**, (2023).
  37. W. J. Venstra, H. J. Westra, H. S. Van Der Zant, Stochastic switching of cantilever motion. *Nat. Commun.* **4**, 2624 (2013).
  38. Y. Liu, Y. Tian, C. Lin, J. Miao, X. Yu, A monolithically integrated microcantilever biosensor based on partially depleted SOI CMOS technology. *Microsyst. Nanoeng.* **9**, 60 (2023).
  39. K. Bera, A. Kiepas, I. Godet, Y. Li, P. Mehta, B. Ifemembi, C. D. Paul, A. Sen, S. A. Serra, K. Stoletov, Extracellular fluid viscosity enhances cell migration and cancer dissemination. *Nature* **611**, 365–373 (2022).
  40. L. Dintenfass, Internal viscosity of the red cell and a blood viscosity equation. *Nature* **219**, 956–958 (1968).
  41. M. Zhang, Z. Zhao, L. Du, Z. Fang, A film bulk acoustic resonator-based high-performance pressure sensor integrated with temperature control system. *J. Micromech. Microeng.* **27**, 045004 (2017).
  42. J. Lee, Z. Wang, K. He, J. Shan, P. X.-L. Feng, Air damping of atomically thin mos2 nanomechanical resonators. *Appl. Phys. Lett.* **105**, 023104 (2014).
  43. J. Peng, G. Song, H. Niu, P. Wang, X. Zhang, S. Zhang, D. Chen, Detection of cardiac biomarkers in serum using a micro-electromechanical film electroacoustic resonator. *J. Micromech. Microeng.* **30**, 075011 (2020).
  44. J. Wang, D. Zhan, K. Wang, W. Hang, The detection of formaldehyde using microelectromechanical acoustic resonator with multiwalled carbon nanotubes-polyethyleneimine composite coating. *J. Micromech. Microeng.* **28**, 015003 (2017).
  45. Z. Zhang, C. Xie, J. Zhang, M. Chan, M. Zhang, Tunable stretchable strain sensors enabled by patterned ecoflex-vertical aligned carbon nanotube arrays and pre-stretching transfer. *Carbon* **197**, 218–225 (2022).
  46. R. Ballerstadt, C. Evans, R. McNichols, A. Gowda, Concanavalin a for in vivo glucose sensing: A biotoxicity review. *Biosens. Bioelectron.* **22**, 275–284 (2006).
  47. Y. Liu, L. Yuan, M. Yang, Y. Zheng, L. Li, L. Gao, N. Nerngchamnon, C. T. Nai, C. S. Sangeeth, Y. P. Peng, Giant enhancement in vertical conductivity of stacked CVD graphene sheets by self-assembled molecular layers. *Nat. Commun.* **5**, 5461 (2014).
  48. D. A. Bryce, J. P. Kitt, J. M. Harris, Confocal raman microscopy for label-free detection of protein–ligand binding at nanopore-supported phospholipid bilayers. *Anal. Chem.* **90**, 11509–11516 (2018).
  49. N. Carney, A. M. Totten, C. O'Reilly, J. S. Ullman, G. W. Hawryluk, M. J. Bell, S. L. Bratton, R. Chesnut, O. A. Harris, N. Kissoon, Guidelines for the management of severe traumatic brain injury, fourth edition. *Neurosurgery* **80**, 6–15 (2017).
  50. J. M. Conly, A. Ronald, Cerebrospinal fluid as a diagnostic body fluid. *Am. J. Med.* **75**, 102–108 (1983).
  51. C. Lin, L. Ryder, D. Probst, M. Caplan, M. Spano, J. LaBelle, Feasibility in the development of a multi-marker detection platform. *Biosens. Bioelectron.* **89**, 743–749 (2017).
  52. L. Wang, S. Xie, Z. Wang, F. Liu, Y. Yang, C. Tang, X. Wu, P. Liu, Y. Li, H. Saijin, S. Zheng, X. Sun, F. Xu, H. Yu, H. Peng, Functionalized helical fibre bundles of carbon nanotubes as electrochemical sensors for long-term in vivo monitoring of multiple disease biomarkers. *Nat. Biomed. Eng.* **4**, 159–171 (2020).
  53. X. Wang, Z. Gong, T. Wang, J. Law, X. Chen, S. Wanggou, J. Wang, B. Ying, M. Francisco, W. Dong, Y. Xiong, J. J. Fan, G. MacLeod, S. Angers, X. Li, P. B. Dirs, X. Liu, X. Huang, Y. Sun, Mechanical nanosurgery of chemoresistant glioblastoma using magnetically controlled carbon nanotubes. *Sci. Adv.* **9**, eade5321 (2023).
  54. International Commission on Non-Ionizing Radiation Protection (ICNIRP), Guidelines for limiting exposure to time-varying electric, magnetic, and electromagnetic fields (up to 300 GHz), International commission on non-ionizing radiation protection. *Health Phys.* **74**, 494–522 (1998).
  55. M. E. Brogan, E. M. Manno, Treatment of malignant brain edema and increased intracranial pressure after stroke. *Curr. Treat. Options. Neurol.* **17**, 327 (2015).
  56. F. Yetkin, U. Kayabas, Y. Ersoy, Y. Bayindir, S. A. Toplu, I. Tek, Cerebrospinal fluid viscosity: A novel diagnostic measure for acute meningitis. *South. Med. J.* **103**, 892–895 (2010).
  57. D. A. Seehusen, M. M. Reeves, D. A. Fomin, Cerebrospinal fluid analysis. *Ann. Fam. Physician* **68**, 1103–1108 (2003).
  58. J. Shin, Y. Yan, W. Bai, Y. Xue, P. Gamble, L. Tian, I. Kandela, C. R. Haney, W. Spees, Y. Lee, M. Choi, J. Ko, H. Ryu, J.-K. Chang, M. Pezhouh, S.-K. Kang, S. M. Won, K. J. Yu, J. Zhao, Y. K. Lee, M. R. MacEwan, S.-K. Song, Y. Huang, W. Z. Ray, J. A. Rogers, Bioreorbable pressure sensors protected with thermally grown silicon dioxide for the monitoring of chronic diseases and healing processes. *Nat. Biomed. Eng.* **3**, 37–46 (2019).
  59. C. Sun, W. Cao, W. Zhang, L. Zhang, Y. Feng, M. Fang, G. Xu, Z. Shao, X. Yang, X. Meng, Design of a ratiometric two-photon fluorescent probe for dual-response of mitochondrial SO<sub>2</sub> derivatives and viscosity in cells and in vivo. *Dyes Pigments* **171**, 107709 (2019).

60. C. J. Seeton, Viscosity-temperature correlation for liquids. *Tribol. Lett.* **22**, 67–78 (2006).
61. D. M. Beurskens, J. P. Huckriede, R. Schrijver, H. C. Hemker, C. P. Reutelingsperger, G. A. F. T. Nicolaes, The anticoagulant and nonanticoagulant properties of heparin. *Thromb. Haemost.* **120**, 1371–1383 (2020).
62. J. C. Pickup, F. Hussain, N. D. Evans, O. J. Rolinski, D. J. S. Birch, Fluorescence-based glucose sensors. *Biosens. Bioelectron.* **20**, 2555–2565 (2005).
63. S. Zhao, C. Shi, H. Hu, Z. Li, G. Xiao, Q. Yang, P. Sun, L. Cheng, W. Niu, J. B. Bi, ISFET and Dex-AgNPs based portable sensor for reusable and real-time determinations of concanavalin A and glucose on smartphone. *Biosens. Bioelectron.* **151**, 111962 (2020).
64. P. Le Floch, S. Meixuanzi, J. Tang, J. Liu, Z. Suo, Stretchable seal. *ACS Appl. Mater. Interfaces* **10**, 27333–27343 (2018).
65. P. Le Floch, S. Zhao, R. Liu, N. Molinari, E. Medina, H. Shen, Z. Wang, J. Kim, H. Sheng, S. Partarrieu, W. Wang, C. Sessler, G. Zhang, H. Park, X. Gong, A. Spencer, J. Lee, T. Ye, X. Tang, X. Wang, K. Bertoldi, N. Lu, B. Kozinsky, Z. Suo, J. Liu, 3D spatiotemporally scalable in vivo neural probes based on fluorinated elastomers. *Nat. Nanotechnol.* 10.1038/s41565-023-01545-6, (2023).
66. J. Steck, J. Kim, Y. Kutsovsky, Z. Suo, Multiscale stress deconcentration amplifies fatigue resistance of rubber. *Nature* **624**, 303–308 (2023).
67. A. D. Mickle, S. M. Won, K. N. Noh, J. Yoon, K. W. Meacham, Y. Xue, L. A. Mcllvried, B. A. Copits, V. K. Samineni, K. E. Crawford, D. H. Kim, P. Srivastava, B. H. Kim, S. Min, Y. Shiuian, Y. Yun, M. A. Payne, J. Zhang, H. Jang, Y. Li, H. H. Lai, Y. Huang, S.-I. Park, R. W. Gereau, J. A. Rogers, A wireless closed-loop system for optogenetic peripheral neuromodulation. *Nature* **565**, 361–365 (2019).
68. S. Sharma, K. B. Ramadi, N. H. Poole, S. S. Srinivasan, K. Ishida, J. Kuosmanen, J. Jenkins, F. Aghlmand, M. B. Swift, M. G. Shapiro, G. Traverso, A. Emami, Location-aware ingestible microdevices for wireless monitoring of gastrointestinal dynamics. *Nat. Electron.* **6**, 242–256 (2023).
69. J. Ausra, S. J. Munger, A. Azami, A. Burton, R. Peralta, J. E. Miller, P. Gutruf, Wireless battery free fully implantable multimodal recording and neuromodulation tools for songbirds. *Nat. Commun.* **12**, 1968 (2021).
70. R. Herbert, H.-R. Lim, B. Rigo, W.-H. Yeo, Fully implantable wireless batteryless vascular electronics with printed soft sensors for multiplex sensing of hemodynamics. *Sci. Adv.* **8**, eabm1175 (2022).
71. T. L. Liu, Y. Dong, S. Chen, J. Zhou, Z. Ma, J. Li, Battery-free, tuning circuit-inspired wireless sensor systems for detection of multiple biomarkers in bodily fluids. *Sci. Adv.* **8**, eabo7049 (2022).
72. Z. Dong, Z. Li, F. Yang, C.-W. Qiu, J. S. Ho, Sensitive readout of implantable microsensors using a wireless system locked to an exceptional point. *Nat. Electron.* **2**, 335–342 (2019).
73. V. Kalidasan, X. Yang, Z. Xiong, R. R. Li, H. Yao, H. Godaba, S. Obuobi, P. Singh, X. Guan, X. Tian, S. A. Kurt, Z. Li, D. Mukherjee, R. Rajarethinam, C. S. Chong, J.-W. Wang, P. L. R. Ee, W. Loke, B. C. K. Tee, J. Ouyang, C. J. Charles, J. S. Ho, Wirelessly operated bioelectronic sutures for the monitoring of deep surgical wounds. *Nat. Biomed. Eng.* **5**, 1217–1227 (2021).
74. X. Chen, B. Assadsangabi, Y. Hsiang, K. Takahata, Enabling angioplasty-ready “Smart” stents to detect in-stent restenosis and occlusion. *Adv. Sci.* **5**, 1700560 (2018).
75. J. Vishnu, G. Manivasagam, Perspectives on smart stents with sensors: From conventional permanent to novel bioabsorbable smart stent technologies. *Med. Devices Sens.* **3**, e10116 (2020).
76. D. K. Piech, B. C. Johnson, K. Shen, M. M. Ghanbari, K. Y. Li, R. M. Neely, J. E. Kay, J. M. Carmena, M. M. Maharbiz, R. Muller, A wireless millimetre-scale implantable neural stimulator with ultrasonically powered bidirectional communication. *Nat. Biomed. Eng.* **4**, 207–222 (2020).
77. S. Sonmezoglu, J. R. Fineman, E. Maltepe, M. M. Maharbiz, Monitoring deep-tissue oxygenation with a millimeter-scale ultrasonic implant. *Nat. Biotechnol.* **39**, 855–864 (2021).
78. M. M. Ghanbari, D. K. Piech, K. Shen, S. F. Alamouti, C. Yalcin, B. C. Johnson, J. M. Carmena, M. M. Maharbiz, R. Muller, A sub-mm<sup>3</sup> ultrasonic free-floating implant for multi-mote neural recording. *IEEE J Solid-State Circuits* **54**, 3017–3030 (2019).
79. A. J. Cortese, C. L. Smart, T. Wang, M. F. Reynolds, S. L. Norris, Y. Ji, S. Lee, A. Mok, C. Wu, F. Xia, N. I. Ellis, A. C. Molnar, C. Xu, P. L. McEuen, Microscopic sensors using optical wireless integrated circuits. *Proc. Natl. Acad. Sci. U.S.A.* **117**, 9173–9179 (2020).
80. M. Han, X. Guo, X. Chen, C. Liang, H. Zhao, Q. Zhang, W. Bai, F. Zhang, H. Wei, C. Wu, Q. Cui, S. Yao, B. Sun, Y. Yang, Q. Yang, Y. Ma, Z. Xue, J. W. Kwak, T. Jin, Q. Tu, E. Song, Z. Tian, Y. Mei, D. Fang, H. Zhang, Y. Huang, Y. Zhang, J. A. Rogers, Submillimeter-scale multimaterial terrestrial robots. *Sci. Robot.* **7**, eabn0602 (2022).
81. X. Wu, Y. Jiang, N. J. Rommelfanger, F. Yang, Q. Zhou, R. Yin, J. Liu, S. Cai, W. Ren, A. Shin, K. S. Ong, K. Pu, G. Hong, Tether-free photothermal deep-brain stimulation in freely behaving mice via wide-field illumination in the near-infrared-II window. *Nat. Biomed. Eng.* **6**, 754–770 (2022).
82. C. Wang, Y. Wu, X. Dong, M. Armacki, M. Sitti, In situ sensing physiological properties of biological tissues using wireless miniature soft robots. *Sci. Adv.* **9**, eadg3988 (2023).
83. X. Yang, W. Shang, H. Lu, Y. Liu, L. Yang, R. Tan, X. Wu, Y. Shen, An agglutinate magnetic spray transforms inanimate objects into millirobots for biomedical applications. *Sci. Robot.* **5**, eabc8191 (2020).
84. H. Lu, M. Zhang, Y. Yang, Q. Huang, T. Fukuda, Z. Wang, Y. Shen, A bioinspired multilegged soft millirobot that functions in both dry and wet conditions. *Nat. Commun.* **9**, 3944 (2018).
85. C. R. Taylor, S. S. Srinivasan, S. H. Yeon, M. K. O'Donnell, T. J. Roberts, H. M. Herr, Magnetometric microscopy. *Sci. Robot.* **6**, eabg0656 (2021).
86. A. Singer, J. T. Robinson, Wireless power delivery techniques for miniature implantable bioelectronics. *Adv. Healthc. Mater.* **10**, e2100664 (2021).
87. X. He, L. Garcia-Gancedo, P. Jin, J. Zhou, W. Wang, S. Dong, J. Luo, A. Flewitt, W. Milne, Film bulk acoustic resonator pressure sensor with self temperature reference. *J. Micromech. Microeng.* **22**, 125005 (2012).
88. V. Rochus, B. Wang, H. A. C. Tilmans, A. Ray Chaudhuri, P. Helin, S. Severi, X. Rottenberg, Fast analytical design of MEMS capacitive pressure sensors with sealed cavities. *Mechatronics* **40**, 244–250 (2016).
89. X. Ji, Y. Fan, T. Han, P. Cai, Nonlinear thickness-stretch vibration of thin-film acoustic wave resonators. *Acoust. Phys.* **62**, 160–164 (2016).
90. W. Kreider, A. Nayfeh, Experimental investigation of single-mode responses in a fixed-fixed buckled beam. *Nonlinear Dynam.* **15**, 155–177 (1998).

**Acknowledgments:** We thank P. Cheng and H. Zhang for providing valuable suggestions.

**Funding:** This work was supported by the National Natural Science Foundation of China (no. 62104009) (to M.H.); the Emerging Engineering Interdisciplinary Project, Peking University, the Fundamental Research Funds for the Central Universities (to M.H.); and Peking Nanofab Laboratory. **Author contributions:** J. Wan and M.H. conceived the idea and designed the research. Z.N. and J. Wan designed the circuits in wearable devices. J. Wan and J.X. carried out the animal experiments with the assistance from S.Y. and W.M. Z.Z., M.Z., and J. Wan performed the surface modification experiment. S.Y. and J. Wan conducted the biocompatibility test. J. Wan, Y.L., and J. Wang developed the deep learning algorithm. J. Wan conducted the benchtop test and calibration test with the assistance from Z.X., X.L., C.X., P.Z., Yiran Wang, J.Z., Yaozheng Wang, and S.Z., J. Wan and M.H. wrote the manuscript, and all authors provided feedback. **Competing interests:** The authors declare that they have no competing interests. **Data and materials availability:** All data needed to evaluate the conclusions in the paper are present in the paper and/or the Supplementary Materials.

Submitted 14 November 2023

Accepted 13 February 2024

Published 20 March 2024

10.1126/sciadv.adm9314